

Integrating few-atom layer metal on high-entropy alloys to catalyze nitrate reduction in tandem

Received: 20 June 2024

Accepted: 11 October 2024

Published online: 18 October 2024



Jiace Hao^{1,8}, Tongde Wang^{2,8}, Ruohan Yu³, Jian Cai¹, Guohua Gao²✉, Zechao Zhuang^{4,5}✉, Qi Kang⁶, Shuanglong Lu¹, Zhenhui Liu⁷, Jinsong Wu³, Guangming Wu², Mingliang Du¹, Dingsheng Wang⁴✉ & Han Zhu¹✉

While high-entropy alloy (HEA) catalysts seem to have the potential to break linear scaling relationships (LSRs) due to their structural complexity, the weighted averaging of properties among multiple principal components actually makes it challenging to diverge from the symmetry dependencies imposed by the LSRs. Herein, we develop a ‘surface entropy reduction’ method to induce the exsolution of a component with weak affinity for others, resulting in the formation of few-atom-layer metal (FL-M) on the surface of HEAs. These exsolved FL-M surpass the confines of the original configurational space of conventional HEAs, and collaborate with the HEA substrate, serving as geometrically separated active sites for multiple intermediates in a complex reaction. This FL-M-covered HEA shows an outstanding performance for electrocatalytic reduction of nitrate to ammonia (NH₃) with a Faradaic efficiency of 92.7%, an NH₃ yield rate of 2.45 mmol h⁻¹ mg_{cat.}⁻¹, and high long-term stability (>200 h). Our work achieves the precise manipulation of atomic arrangement, thereby expanding both the chemical space occupied by known HEA catalysts and their potential application scenarios.

Electrochemical synthesis of chemicals and fuel feedstocks, such as alkanes, alcohols, and ammonia, usually involves multiple electron and proton transfers and competing adsorption of different intermediates^{1–3}. However, there exists a linear correlation among the adsorption energies of different intermediates on the electrocatalyst surface, posing a dilemma of how to simultaneously enhance the electrocatalyst’s activity toward all reaction intermediates of multistep transformations⁴. Such a so-called scaling relationship leads to a scenario where the more complex the reaction, the more challenging the design of the electrocatalyst becomes⁵.

Throughout the history of electrocatalyst development for sustainable electrosynthesis, metal complexes, metal nanoparticles, alloys or intermetallics, nanoclusters, single-atom catalysts, and high-entropy alloys (HEAs) emerged successively, with each of them becoming representative electrocatalysts of their respective eras^{6–8}. Among them, HEAs stand out with their multicomponent surface, tailorable compositions, and unique ‘cocktail’ effects, making them an almost ideal electrocatalyst design with diverse active sites to individually bind, polarize, and activate substrates and intermediates, leading to the final product^{9,10}. The potential of HEAs to catalyze a range of

¹Key Laboratory of Synthetic and Biological Colloids, Ministry of Education, School of Chemical and Material Engineering, Jiangnan University, Wuxi, China.

²Shanghai Key Laboratory of Special Artificial Microstructure Materials and Technology, Key Laboratory of Road and Traffic Engineering of the Ministry of Education, Tongji University, Shanghai, China. ³Nanostructure Research Centre, Wuhan University of Technology, Wuhan, P. R. China. ⁴Department of Chemistry, Tsinghua University, Beijing, P. R. China. ⁵Department of Chemical Engineering, Columbia University, New York, NY, USA. ⁶Institute of New Energy for Vehicles, School of Materials Science and Engineering, Tongji University, Shanghai, China. ⁷College of Material Science and Engineering, Nanjing University of Aeronautics and Astronautics, Nanjing, P. R. China. ⁸These authors contributed equally: Jiace Hao, Tongde Wang. ✉e-mail: gao@tongji.edu.cn; zhuangzc@mail.tsinghua.edu.cn; wangdingsheng@mail.tsinghua.edu.cn; zhysw@jiangnan.edu.cn

electrochemical reactions, such as water electrolysis for hydrogen production, carbon dioxide electrolysis to generate hydrocarbons and alcohols, and nitrogen/nitrate reduction for ammonia synthesis, has been demonstrated over the past few years^{11–17}. While HEA electrocatalysis constitutes a whole new paradigm, the vastness of compositions in HEAs, which is orders of magnitude larger than that of bi- and trimetallic alloys, becomes intractable^{18–20}. More importantly, the weighted averaging of properties among surface metal atoms drives the convergence of adsorption energies of reactants on these atoms toward a common value, indicating that HEAs obey similar scaling relations to other well-established heterogeneous catalyst systems. Therefore, the necessity of an improved design of HEA electrocatalysts through precise manipulation of atomic arrangement beyond the confines of the original configurational space is apparent.

Herein, we develop a ‘surface entropy reduction’ approach to break the scaling relationship inherent in conventional HEAs by in situ exsolving FL-M from the surface as new active sites. Specifically, using entropy balancing in an open HEA system, a principal component element with weak affinity for others, for example, silver, can be exsolved on the surface, resulting in the formation of few-atom-layer silver (FL-Ag). These FL-Ag interact with neighboring metal sites on the HEA parent to establish new active-site motifs, which avoid the generally encountered scaling relationships and, therefore, enable highly efficient cascade conversion of nitrate into ammonia. Combined in situ characterizations and first-principles simulations confirm the critical role of FL-Ag in promoting the continuous generation of the NO intermediate and its subsequent reduction over the HEA nearby. This FL-Ag/HEA catalyst demonstrates outstanding performance, achieving a Faradaic efficiency of 92.7%, an NH₃ yield rate of 2.45 mmol h^{−1} mg_{cat}^{−1}, and notable long-term stability (> 200 h), far outperforming conventional HEA. Our work demonstrates a low-entropy HEA surface with a high level of chemical complexity and opens up more opportunities to improve the catalytic performance of HEA catalysts toward sustainable ammonia production.

Results

Calculation-assisted HEA electrocatalyst designs

The electrochemical nitrate reduction reaction (NitRR) involves the transfer of eight electrons and alternating deoxygenation and hydrogenation reactions²¹, and the *NO₃, *NO, and *NOH are the key intermediates in the NitRR. Three factors should be prioritized to design advanced NitRR electrodes with high FE and yield: (1) provide binding sites with wide adsorption energy distributions that could regulate various intermediates for complex reactions. (2) optimize the energy barriers for the rate-determining step (RDS), such as *NO₃ and *NO hydrogenation; (3) balance the energy barriers for NitRR and competitive hydrogen evolution reaction (HER). We first performed DFT calculations to evaluate the reaction-free energies for NitRR and reaction pathways and corresponding adsorption configurations of various intermediates generated during NitRR process over a series of mono metals (Fe, Co, Ni, V, Ag, Pd, Cu, Ru, Zn, and Sn) were shown in Supplementary Fig. 1. The models for mono metal Ag, single-phase FeCoNiVAgPd HEA (HEA_{homo}), and FL-Ag/HEA were constructed using the experimental results and constitutive entropy equation (details in Supplementary Note 1, Supplementary Data 1 and Supplementary Fig. 2). The free energies of *NO₃, *NO₂, *NO, *NOH, *NH intermediates over each monometals show typical linear scaling relations (Fig. 1a). It means that the hydrogenation barrier associated with scaling relationships on a single-metal active site catalyst always exist during the NitRR. In comparison, as shown in Fig. 1b, the designed HEA_{homo} could simultaneously provide the weak adsorption sites for *NO (Ag and Pd) and the strong adsorption sites for *NOH (Fe, Co, Ni, V) (Supplementary Note 2 and Supplementary Fig. 4). These significant differences in adsorption strength of *NO and *NOH would lead to the greatly decrease in energy barrier of *NO hydrogenation. HEA_{homo} with

tunable metal sites can adjust the adsorption strength of different intermediates to boost the activity of complex NitRR by breaking the inherent linear relationship that existed in mono metals.

The *NO₃ hydrogenation over HEA_{homo} is endothermic, and there need two metal atoms to stabilize the adsorption *NO₃. The free energy changes for *NO₃ hydrogenation (*NO₃ to *HNO₃ (ΔG_{HNO_3}) on different metal sites (e.g., Fe, Co, Ni, V, Ag, and Pd) indicate that the Ag-Ag site shows the lowest energy barrier of 0.38 eV (Fig. 1c), with the highest amount of electrons transferred between the H atom and NO₃ (0.85 e, Supplementary Fig. 4). However, HEA_{homo} with randomly element distribution is difficult to afford enough Ag-Ag sites for the stabilization of *NO₃, which is inevitably affected by the surrounding Fe/Co/Ni/Pd/V sites with strong absorption strength (Supplementary Fig. 5). Therefore, we designed FL-Ag/HEA by regulating the surface element distribution of HEA to achieve the relative proportion of Ag-Ag sites on HEA surfaces.

The adsorption energy of N atoms can be used to describe the adsorption of the whole NitRR reaction on the catalyst surface, due to the positive correlation with the adsorption energies of all the reaction intermediates involved in NitRR (Supplementary Fig. 3). Therefore, we used binding energy distribution pattern (BEDP) to determine the features of the customized FL-Ag/HEA catalysts for complex reactions that involved multiple intermediates (Fig. 1d). The horizontal coordinate is the adsorption energy strength of the N atoms while the vertical coordinate is the number of sites with this adsorption strength. The mono-metal phase shows a single adsorption site and cannot provide appropriate adsorption strength for all intermediates during NitRR (the gray line in the diagram). The surface distribution of HEA_{homo} provides a broad adsorption energy distribution range that provides the possibility to regulate multiple intermediates at the same time. Interestingly, by precisely controlling the entropy value of the system to form FL-Ag/HEA, we can controllably increase the number of metal sites with better catalytic activity (such as Ag-Ag) to react in key steps (such as NO₃[−] hydrogenation), thereby further improving the catalytic activity by breaking the scaling relations.

Synthesis and characterizations of FL-Ag on HEA

The abovementioned FL-Ag/HEA were designedly and synthesized via a ‘surface entropy reduction’ strategy. The Ag metal exhibits high DH_{mix} with each of Fe, Co, Ni, V, and Pd, suggesting the poor compatibility of Ag with other metals at common conditions (Supplementary Fig. 6). The single-phase FeCoNiVAgPd HEA_{homo} nanoparticles (NPs) only achieved at high temperatures (1200 °C) while the immiscible Ag can exsolve from the inner HEA phase to form FL-Ag on HEA surfaces under low temperature (1000 °C). Supplementary Fig. 7 depicts the nanofiber-mediated synthesis procedure of the FL-Ag/HEA and HEA_{homo}. HEA_{homo} NPs immobilized on CNFs exhibit near-spherical morphology with sizes of 20–50 nm (Fig. 2a and Supplementary Fig. 8a). Evidenced by X-ray diffraction (XRD), the HEA_{homo} is attributed to the face-centered cubic (fcc) phase (JPCDS: Ni-04-0850, Supplementary Fig. 9). The low and high magnification elemental maps confirm the HEA_{homo} NP with homogeneous distribution of Fe, Co, Ni, Cu, Ag and Pd (Fig. 2b). The atomic-resolution high-angle annular dark-field scanning transmission electron microscopy (HAADF-STEM) collected on the surface of HEA_{homo} NP shows the d-spacings of 2.17 Å assigned to the (111) planes of fcc HEA phase (Figs. 2c, d).

FL-Ag/HEA were obtained at 1000 °C (Fig. 2e and Supplementary Fig. 8b) and the elemental maps of a FL-Ag/HEA NP clearly show the dispersed FL-Ag on the outer rims of the FeCoNiCuAgPd HEA core (Fig. 2f). Atomic-resolution HAADF-STEM (Figs. 2g, 2h) exhibit the 0.6 nm thick FL-Ag form coherent interfaces with the HEA core. Low-magnification HAADF-STEM images collected on different edge regions of FL-Ag/HEA clearly demonstrate that the FL-Ag were randomly dispersed on HEA surfaces rather than forming a complete Ag shell (Supplementary Fig. 10). Supplementary Fig. 11 shows the

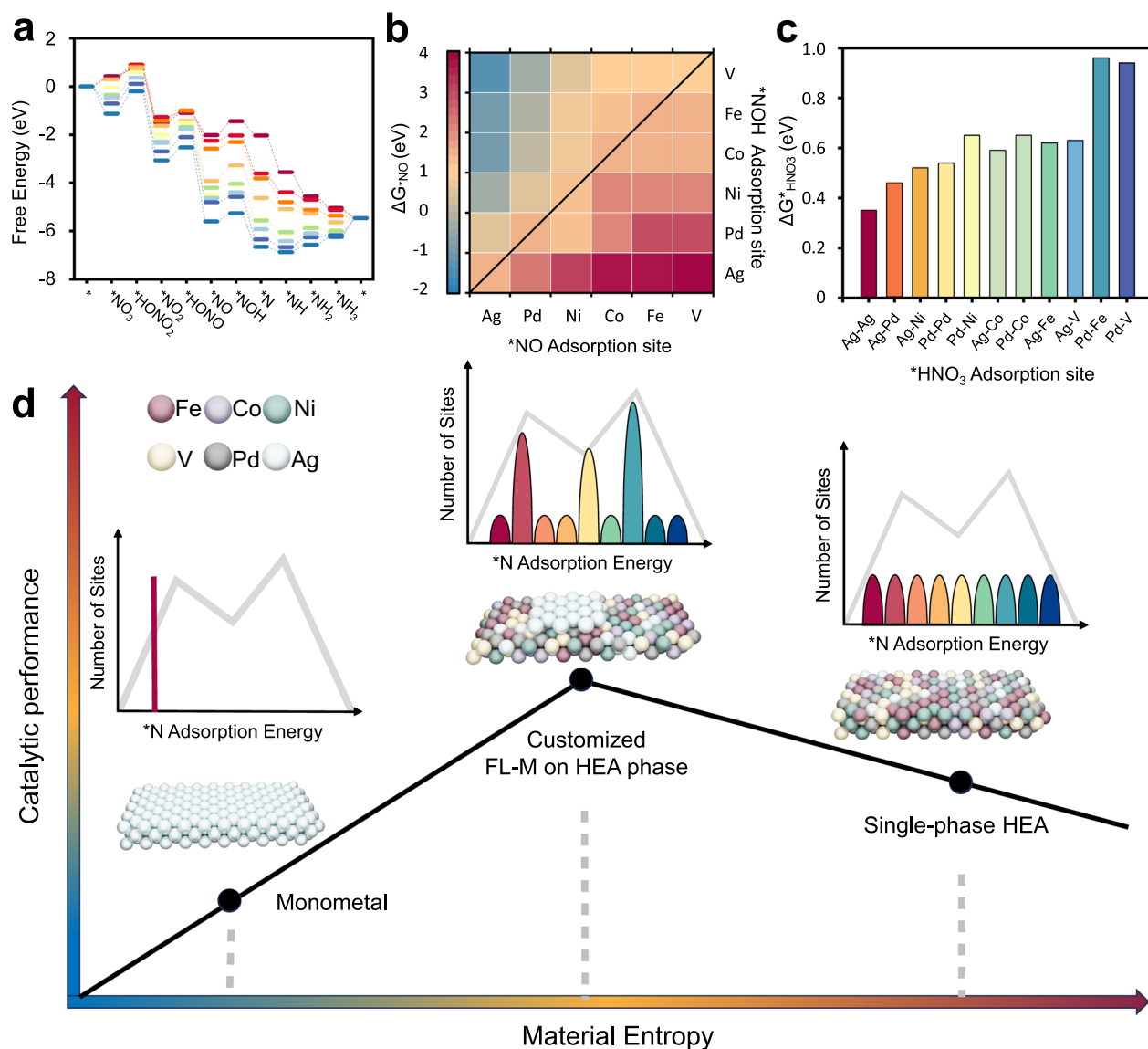


Fig. 1 | Aim of this work. a Reaction free energies for NitRR over different monometals. **b** Free energy changes of *NO hydrogenation ($\Delta G_{^*NO}$) on different combinations of metal sites in HEA_{homo} . **c** Free energy changes of *NO_3

hydrogenation ($\Delta G_{^*HNO_3}$) on different metal sites in HEA_{homo} . **d** The electrocatalytic activity of designed monometal, HEA_{homo} , and customized FL-Ag/HEA catalysts with increased materials entropy.

randomly selected atomic resolution HAADF-STEM images of FL-Ag/HEA NPs, and they both demonstrate the incomplete FL-Ag on HEA surfaces. XRD patterns of FL-Ag/HEA/CNFs demonstrate the coexistence of fcc Ag and fcc HEA crystals (Supplementary Fig. 9). The clear diffraction spots of (111) and (200) lattice planes of Ag were revealed by fast Fourier transform (FFT) pattern of FL-Ag/HEA while the HEA_{homo} only exhibit the superlattice points for the fcc HEA (Supplementary Fig. 12). Molecular dynamics (MD) simulated structural evolution of HEA-FL-Ag interfaces within 8 ps at 1200 °C further demonstrate that more heat transfer leads to diffusion of atoms from HEA phase into the FL-Ag through the HEA-FL-Ag interfaces (Fig. 2i-l and Supplementary Data 1), which was according with the STEM results. The in-plane (E_{xx}) and out-of-plane (E_{yy}) strain field maps of HEA_{homo} and FL-Ag/HEA obtained by geometrical phase analysis (GPA) indicate the noticeable changes in lattice strain throughout the surface region of FL-Ag/HEA (Supplementary Fig. 13). This means that the overlay has a new lattice structure (FL-Ag) that is mismatched with the HEA_{homo} .

The Ag and HEA atomic columns were further identified via the statistical parameter estimation theory based on the refined ideal crystal lattices (experimental section)^{22,23}. The atomically resolved strain maps of the (111) planes were derived by calculating the displacement of the measured atomic arrangement relative to the theoretical positions (Supplementary Figs. 14 and 15). HEA_{homo} exhibits relatively tiny and uniform strain due to the slightly compressed outermost layer atoms (Fig. 3a). In FL-Ag/HEA (Fig. 3b) because the HEA unit cell is smaller than that of Ag, the HEA columns show increasing tensile strain when approaching the HEA-Ag interfaces while the FL-Ag is compressed compared with the individual Ag phase. The distinct differences between the strain maps of HEA_{homo} and FL-Ag/HEA further show the unique coherent HEA-Ag interfaces between the outer FL-Ag and HEA core. The corresponding intensity profiles of HEA/Ag_{homo} (Fig. 3c) and FL-Ag/HEA (Fig. 3d) show considerable differences in the d-spacing of (111) planes for the FL-Ag and HEA core. Three-dimensional (3D) models and atomic ratios of Fe/Co/Ni/V/Ag/Pd in HEA/Ag_{homo} and FL-Ag/HEA are shown in Fig. 3e, and the redistribution

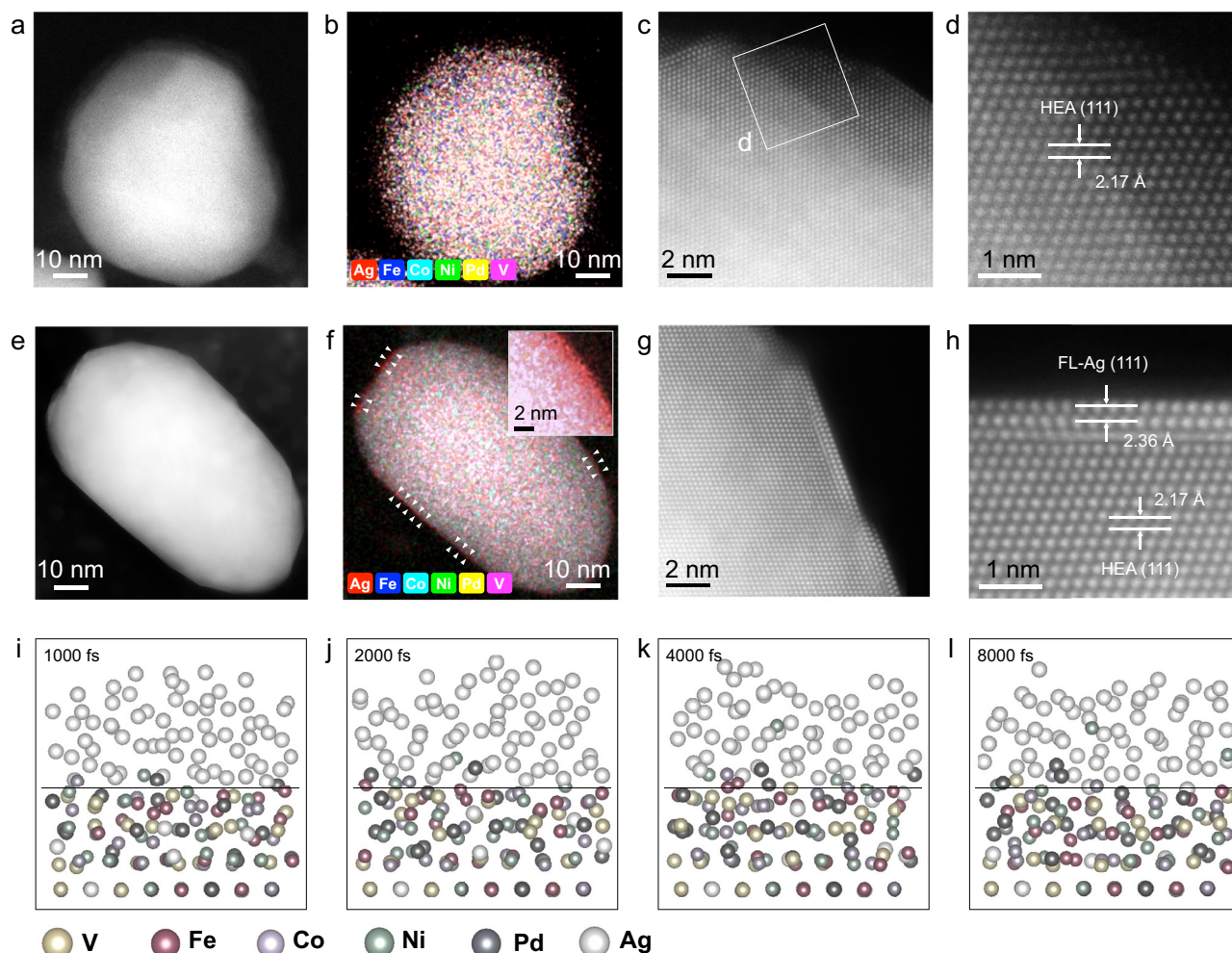


Fig. 2 | Structural characterizations. HAADF-STEM images, STEM-EDS mapping images, and atomic-resolution HAADF-STEM images of the (a–d) HEA_{homo} and (e–h) FL-Ag/HEA NPs supported on CNFs. Fig. 2d is the enlarged area in 2c. i–l MD simulated structural evolution of HEA–FL-Ag interfaces within 8 ps at 1200 °C. The

red dotted line is the original dividing line between the HEA phase and the FL-Ag, and the marked blue circles are the diffusion atoms from the HEA phase into the FL-Ag.

of Ag from FL-Ag/HEA to HEA_{homo} exhibits consistent atomic ratios, as measured via inductively coupled plasma optical emission spectrometry (ICP-OES, Supplementary Table 1).

X-ray absorption near-edge structure (XANES) spectra (Supplementary Fig. 16) unveil the relatively high valence of Ag in FL-Ag/HEA but remains in a metallic state. Together with the positive shifts of Ag 3d binding energies of FL-Ag/HEA detected by X-ray photoelectron spectroscopy (XPS), it indicates that more electron transfer occurs from FL-Ag to surrounded metal atoms in the HEA phase when compared with those of HEA_{homo} (Supplementary Fig. 17). We further performed the Pd 3d and Ag 3d XPS depth profiles of FL-Ag/HEA and HEA_{homo}. As shown in Supplementary Fig. 18, the Ag 3d XPS depth profiles of FL-Ag/HEA indicate that with the increased etching depth, the BEs for Ag⁰ 3d_{3/2} and Ag⁰ 3d_{5/2} of FL-Ag/HEA exhibit positive shifts (0.3 eV) to relatively higher values, while the BEs for Ag⁰ 3d_{3/2} and Ag⁰ 3d_{5/2} of HEA_{homo} display no shift. Specifically, the results indicate unique electron states of FL-Ag, which is different from that of Ag of the HEA phase. Meanwhile, the BEs for Pd 3d XPS of FL-Ag/HEA emerged at 341.4 and 336.2 eV, which is, accordingly, with that of HEA_{homo}, demonstrating that the HEA phase is not completely covered by the FL-Ag. The Pd 3d XPS depth profiles of FL-Ag/HEA and HEA_{homo} demonstrate that the BEs for Pd⁰ 3d_{3/2} and Pd⁰ 3d_{5/2} in FL-Ag/HEA and HEA_{homo} appeared at 341.4 and 336.2 eV, respectively, do not change

regardless of the increased depth. The above results strongly demonstrate the formation of FL-Ag/HEA structures.

The k²-weighted Fourier-transformed (FT) extended X-ray absorption fine structure (EXAFS) shows that in the R space, FL-Ag/HEA exhibits prominent peaks at 2.62 Å, assigned to the Ag–Ag scattering path, whereas the HEA_{homo} and Ag foil exhibits peaks for Ag–Ag at ~2.60 and ~2.65 Å (Fig. 3g). The EXAFS fitting further shows a quantitative structural configuration of Ag in FL-Ag/HEA. The Ag–M (M = Fe, Co, Ni, Ag, Pd) bonds in FL-Ag/HEA contain Ag–Ag/Pd and Ag–Fe/Co/Ni bonds. The coordination number (CN) of Ag atoms in FL-Ag/HEA is 9.4, whereas the CN of Ag in Ag foil and HEA_{homo} are 9.9 and 12, respectively. The detailed fitting parameters are shown in Supplementary Table 2. The wavelet transform (WT) of K-edge EXAFS spectra (Supplementary Fig. 19) in Ag foils shows a maximum intensity at ~9.0 Å^{–1}, which is attributed to Ag–Ag bonding. In contrast, the WT contour plots of FL-Ag/HEA and HEA_{homo} exhibit maximum intensities at 9.2 and 8.7 Å^{–1}. The Ag–Ag bonds are dominant in FL-Ag/HEA because of the presence of the FL-Ag, and the Ag in the HEA_{homo} attenuates the signals of Ag–Fe/Co/Ni bonds. These results strongly support the contention that the FL-Ag formed on HEA surfaces due to the quite differences of Ag–Ag bonds in FL-Ag/HEA and HEA_{homo}.

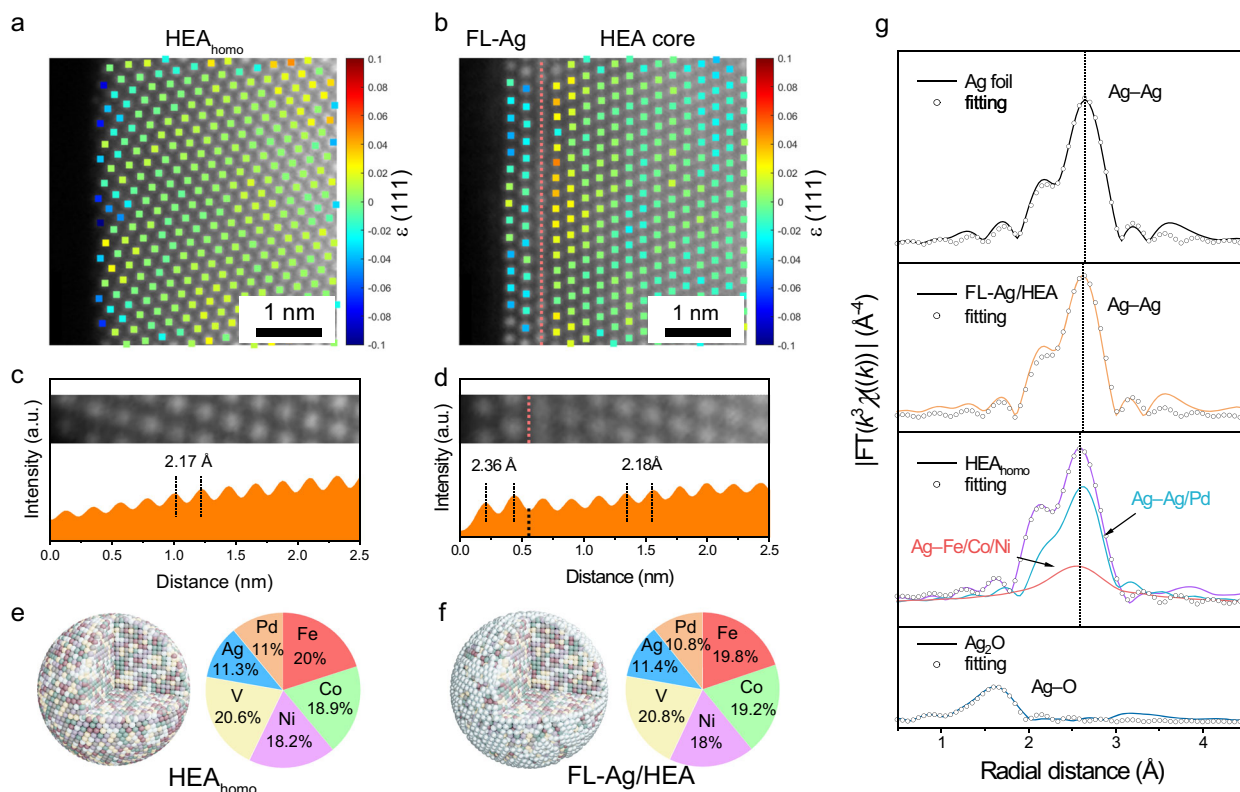


Fig. 3 | Atomic structure analysis. Atomically resolved strain maps of the (111) planes in (a) HEA_{homo} and (b) FL-Ag/HEA derived via the statistical parameter estimation theory. The nanointerface is marked using the red dotted line. Corresponding intensity profiles of the (111) planes in (c) HEA_{homo} and (d) FL-Ag/HEA NPs.

3D models of (e) FL-Ag/HEA and (f) HEA_{homo} with the atomic percentage of constituent elements shown in the pie charts. **g** FT-EXAFS and corresponding fitting spectra of FL-Ag/HEA/CNFs, HEA_{homo}/CNFs, Ag, and Ag₂O foils.

NitRR performance

We measured the NitRR performances in a standard three-electrode H-type cell separated by an ion-exchange membrane (Nafion 117) under ambient conditions using FL-Ag/HEA/CNFs and HEA_{homo}/CNFs and Ag/CNFs directly as an electrode (geometric area = 1 cm²). The FEs and yield rates for products were derived from chronoamperometry measurements (*i*-*t* curves) (Supplementary Fig. 20), and quantified by ultraviolet–visible (UV–vis) spectrophotometry with calibration curves (Supplementary Figs. 21 and 22). The linear sweep voltammetry (LSV) curves indicate the significantly enhanced current densities collected on FL-Ag/HEA/CNFs in 0.5 M K₂SO₄ with 0.1 M KNO₃ (Fig. 4a), and furthermore, the NH₃ is undetectable in 0.5 M K₂SO₄ without NO₃[−] (Supplementary Fig. 23), demonstrating its high intrinsic activity for NitRR. FL-Ag/HEA/CNFs exhibit the highest total current density (Fig. 4b) and partial NH₃ current density (Supplementary Fig. 24) compared to Ag/CNFs and HEA_{homo}/CNFs. In addition, the LSV curves of FL-Ag/HEA/CNFs show different slopes in different potential ranges because of the step-by-step reduction of NO₃[−]. Herein, the deoxidation of NO₃[−] to *NO_x mainly occurs in the potential range from 0.5 to −0.15 V (region I), whereas the hydrogenation of intermediates occurs from −0.15 to −0.57 V (region II)^{24,25}. The LSV results demonstrate the strong capability of FL-Ag for regulating the NO₃[−] reduction to *NO_x, which cannot be observed in HEA_{homo}. As shown in Fig. 4c, Ag/CNFs exhibit high NO₂[−] FEs low potential, indicating that Ag actively participates in NO₃[−] hydrogenation to NO₂[−] rather than NH₃. The NH₃ FEs of FL-Ag/HEA/CNFs exhibit volcanic-shaped curves with a maximum value of 92.7% at −0.57 V vs. RHE without iR compensation, which is higher than that of HEA_{homo}/CNFs (80.8%). HEA_{homo}/CNFs exhibit relatively high H₂ FEs in the whole potential range, suggesting the poor capability for suppressing the HER. H₂ is the sole gas product determined by gas chromatography. Such a high FE (NH₃) of 92.7% and NH₃

yield rate of 0.29 mmol h^{−1} cm^{−2} at very low potential are achieved by FL-Ag/HEA structures, indicating the key role of FL-Ag for the NitRR (Fig. 4d).

The control experiment was conducted at the open circuit potential, NH₃ is undetectable over FL-Ag/HEA/CNFs as reflected in the UV–Vis spectra (Supplementary Fig. 25), indicating that NH₃ is produced via the electrocatalytic process instead of environmental contamination. The negligible current and NH₃ yield rate of bare CNFs (Supplementary Fig. 26) exclude the influence of the support. To prove whether the NH₃ produced from the FL-Ag/HEA/CNFs-catalyzed NitRR, the isotope-labeling validation experiments were performed using K¹⁵NO₃ and K¹⁴NO₃ as resources at −0.57 V vs. RHE over a 2 h reaction period. Typical doublet peaks of ¹⁵NH₄⁺ and triplet peaks of ¹⁴NH₄⁺ were detected without any additional peaks (Supplementary Figs. 27 and 28). In addition, the nearly identical NH₃ FEs and yield rates of ¹⁴NH₄⁺ and ¹⁵NH₄⁺ quantified by both the ¹H NMR method and indophenol blue method imply that the detected NH₃ produced indeed from the FL-Ag/HEA/CNFs-catalyzed NitRR (Fig. 4e).

The double-layer capacitance (*C*_{dl}) estimated via cyclic voltammetry measurements of the FL-Ag/HEA/CNFs is 99.63 mF cm^{−2}, which is similar to that of HEA_{homo}/CNFs (89.63 mF cm^{−2}) because of the comparable sizes of these electrocatalysts (Supplementary Fig. 29). FL-Ag/HEA/CNFs still exhibits the highest electrochemically active surface area (ECSA)-normalized *J*_{NH₃}, followed by HEA_{homo}/CNFs and Ag/CNFs (Supplementary Fig. 30), indicating its high intrinsic activity for the NitRR. Electrochemical impedance spectroscopy shows the small charge transfer resistance (*R*_{ct}) recorded on FL-Ag/HEA/CNFs (43.4 Ω), demonstrating the fast NitRR kinetics (Supplementary Fig. 31), which shows the importance of FL-Ag as they modify the electronic structure of FL-Ag/HEA. The NitRR performance over FL-Ag/HEA/CNFs was further studied at different NO₃[−] concentrations (50, 100, 500, and

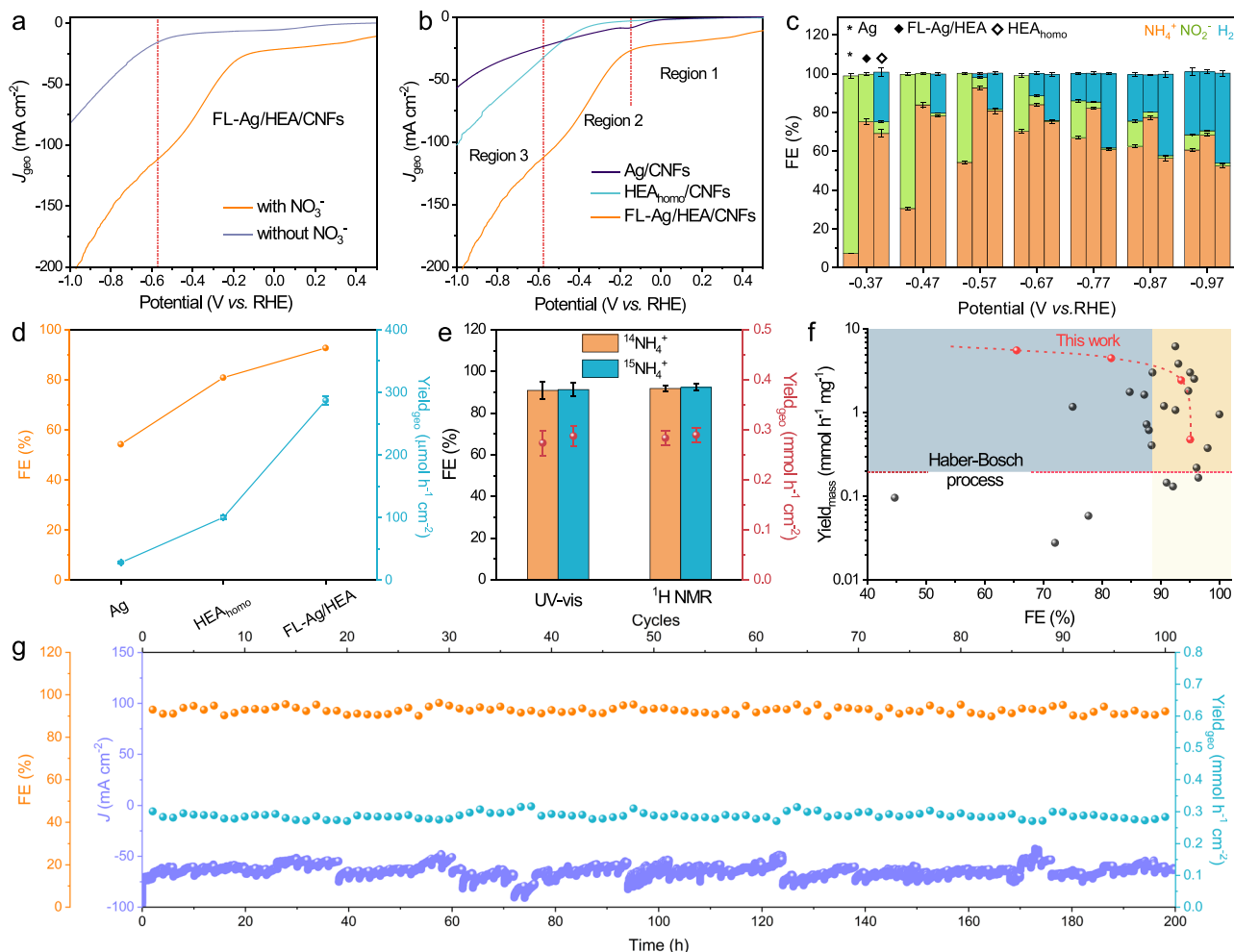


Fig. 4 | Electrocatalytic NitRR performance. **a** LSV curves of FL-Ag/HEA/CNFs normalized to the geometric area in 0.5 M K₂SO₄ with and without 0.1 M KNO₃ at a scan rate of 5 mV s⁻¹ (without iR compensation). **b** LSV curves and **(c)** NitRR products FEs of Ag/CNFs, FL-Ag/HEA/CNFs and HEA_{homo}/CNFs obtained at different potentials in 0.5 M K₂SO₄ with 0.1 M KNO₃. **d** Comparison of the NH₃ production rates of Ag/CNFs, FL-Ag/HEA/CNFs, and HEA_{homo}/CNFs at -0.57 V vs. RHE. **e** NH₃ FEs and yield rates on FL-Ag/HEA/CNFs obtained via UV-vis and NMR spectroscopy using ¹⁵NO₃⁻ and ¹⁴NO₃⁻ as the nitrogen sources. **f** Comparison of the NH₃ production rates on FL-Ag/HEA/CNFs with extensively reported NitRR electrocatalysts

based on the metal content. The yield_{mass} was evaluated by dipping the FL-Ag/HEA/CNFs catalyst ink on the glassy carbon electrode (GCE) electrode. The catalyst loading is 0.015 mg, and the mass loading of the active metal component is 0.0023 mg. **g** Long-term stability test (200 h) of FL-Ag/HEA/CNFs at 75 mA cm⁻² in 0.5 M K₂SO₄ containing 0.1 M KNO₃ in an H cell. Corresponding NH₃ FEs and production rates on FL-Ag/HEA/CNFs during 100 cycles of the electrocatalytic NitRR. Error bars correspond to the standard deviations calculated by performing three independent measurements.

1000 mM NO₃⁻, Supplementary Fig. 32). It is reported that achieving a high ammonia FE is challenging because of the dominant competing HER at low NO₃⁻ concentrations. Inspiringly, FL-Ag/HEA/CNFs maintain their high ammonia FE and yield rate at low NO₃⁻ concentrations, which are ~92% and 0.29 mmol h⁻¹ cm⁻², respectively. The mass activity of FL-Ag/HEA/CNFs was measured to compare its NitRR performance with that of recently reported advanced electrocatalysts. FL-Ag/HEA/CNFs exhibits a high NH₃ FE of 92.7% and an NH₃ yield rate of 2.45 mmol h⁻¹ mg_{cat}⁻¹ (details in experimental section), outperforming most of the state-of-the-art electrocatalysts and traditional Haber-Bosch process for NH₃ production (0.2 mmol h⁻¹ mg_{cat}⁻¹) (Fig. 4f and Supplementary Table 3)²⁶. FL-Ag/HEA/CNFs also show strong performance in alkaline electrolytes (1.0 M KOH + 0.1 M KNO₃), achieving a high FE of 90.5% and yield rate of 0.207 mmol h⁻¹ cm⁻² (Supplementary Fig. 33). The long-term stability of FL-Ag/HEA/CNFs in an H cell was determined by performing 100 continuous electrolytic cycles, and a current density of 75 mA cm⁻² at -0.57 V over FL-Ag/HEA/CNFs remained stable for 200 h and a >92% NH₃ FE and 0.29 mmol h⁻¹ cm⁻² was retained (Fig. 4g). The morphology and structure of FL-Ag/

HEA after stability tests remain unchanged, as proven by LSV curves, EIS spectra, HAADF-STEM, STEM-EDS, Raman, and XRD results (Supplementary Figs. 34–39). As shown in Supplementary Table 4, only the Fe element (0.011 ppm) can be detected in the electrolyte after the long-term test, as determined by ICP-OES. The contents of the other metal elements in the electrolyte were below the detection limit (0.01 ppm), suggesting the extraordinary stability of FL-Ag/HEA.

Relay catalysis mechanism over FL-Ag/HEA

Online differential electrochemical mass spectrometry (DEMS) was used to capture possible intermediates during the NitRR process on FL-Ag/HEA (Supplementary Fig. 40). Fig. 5a shows the m/z signals of NO₂ (46), NH₂OH (33), NO (30), NOH (31), N (14), NH (15), and NH₂ (16), which are detected as the dominating intermediates of the NitRR. The NitRR process on FL-Ag/HEA follows a concerted proton-electron transfer (CPET) pathway of NO₃⁻ → *NO₃ → *NO₂ → *NO₂H → *NO → *NOH → *N → *NH → *NH₂ → *NH₃ → NH₃ because of the extremely weak m/z signals of NH₂OH (Supplementary Fig. 41)²⁷. Electrochemical in situ Raman spectra (Supplementary Fig. 42) of FL-Ag/HEA show the emergence of N-H

characteristic peak (779 cm^{-1}) in a 0.1 M NO_3^- electrolyte^{28,29}, but no N–H peaks are detected in the electrolyte without NO_3^- (Supplementary Fig. 43), confirming the proceeded NitRR catalyzed by FL-Ag/HEA. In addition, no Raman peaks corresponding to Ag oxide or other metal oxide are observed in the applied voltage range from 0.68 to -1.32 V , indicating the stable structure of FL-Ag/HEA. Furthermore, Supplementary Fig. 44 displays the in situ Raman spectra of FeCoNiVAg/CNFs without Pd element. There were no characteristic Raman peaks for $^*\text{NH}$ species observed in the range of $600\text{--}900\text{ cm}^{-1}$, indicating that the Pd element plays a vital role for promoting the NitRR process.

In situ attenuated total reflectance Fourier transform infrared (ATR-FTIR) spectroscopy was further used to identify the absorbed intermediates (Supplementary Fig. 45). The FTIR spectrum acquired at a reference potential of 0.68 V (E_{R}) was used as the reference spectrum (R_{ref}). As shown in Fig. 5b, c, the peaks at ~ 3520 and 1670 cm^{-1} are ascribed to the O–H stretching and bending modes of H_2O , respectively³⁰. The sharp peak centered at 1229 cm^{-1} is attributed to the desorption of sulfonate (SO_3^-) of Nafion in the potential range from 0.68 to -1.32 V ³¹. The characteristic peaks of H^+ at $\sim 2045\text{ cm}^{-1}$ are only detected on FL-Ag/HEA, which shows the stronger adsorption of H^+ on FL-Ag/HEA than HEA_{homo} ^{25,32}. The characteristic peaks at 3610 and 3520 cm^{-1} are attributed to the O–H stretching vibration of N–OH intermediates and adsorbed H_2O on FL-Ag/HEA surfaces. The continuous generation of N–OH and consumption of H_2O show the high conversion efficiency from NO_3^- to NH_3 of FL-Ag/HEA even at more negative potentials. The O–H peak of adsorbed H_2O shifts to a lower wavenumber at 3350 cm^{-1} , showing that more and more OH is generated on HEA_{homo} surfaces. The weak N–OH peak in the FTIR spectrum also indicates the rapid HER process and hindered the deoxidation process over HEA_{homo} . These results proved that the combined HEA–FL-Ag interfaces can regulate the HER process, boosting the NH_3 selectivity.

The presence of the peaks of N–H antisymmetric bending, N–H in-plane shearing, $-\text{NH}_2$ wagging, and $-\text{NH}_2$ rocking modes at 1667 , 1444 , 1307 , and 1105 cm^{-1} proves the generation of NH_3 (Figs. 5d, e)^{30,33}. The peak of the N–O stretching vibration from NO_3^- on FL-Ag/HEA surfaces starts to appear at a very small potential of 0.58 V ^{34,35}. In contrast, the N–O peak begins to appear with a more negative potential of 0.1 V , confirming that the strong NO_3^- absorption ability of FL-Ag makes the NitRR process more favorable on FL-Ag/HEA than HEA_{homo} . In addition, the upward N–O peak corresponding to the consumption of NO_3^- and the downward N–H peak corresponding to the formation of NH_3 indicate the conversion from NO_3^- to NH_3 . The N–O asymmetric vibration mode corresponding to the absorbed NO intermediate (1589 cm^{-1}) exhibits a decreasing intensity at the potential ranges from 0.58 to -0.32 V , indicating the continuous generation of the NO intermediate on FL-Ag/HEA surfaces^{36,37}. Interestingly, the N–O peak shifts to higher wavenumbers of 1612 cm^{-1} when the potential is negatively increased to -0.32 V . These peak shifts can be attributed to the changes in the bonding metal site of NO_2 intermediates on FL-Ag/HEA surfaces. No peak shift for N–O was detected on HEA_{homo} , and these results indicate the presence of relay catalysis for the NitRR over different sites in FL-Ag/HEA.

We further used the DFT calculations to unravel the relay catalysis mechanism on FL-Ag/HEA (“Methods”). The adsorption energies (E_{a}) of key intermediates (i.e., $^*\text{NO}_3$, $^*\text{NO}$, $^*\text{NOH}$, and $^*\text{NH}_3$) on individual metal sites in FL-Ag/HEA (Fig. 6a) and HEA_{homo} (Supplementary Note 3 and Supplementary Fig. 46) were determined, and all E_{a} follow the order of $\text{Ag} < \text{Pd} < \text{Ni} < \text{Co} < \text{Fe} < \text{V}$. Therefore, the NitRR pathways were calculated on representative weak adsorption (Ag and Pd), moderate adsorption (Co), and strong adsorption (V) sites on the surface of FL-Ag/HEA and HEA_{homo} . As shown in Fig. 6b, the energy barrier for $^*\text{NO}_3$ hydrogenation ($^*\text{NO}_3$ to $^*\text{HNO}_3$) on surface Ag sites of FL-Ag/HEA shows a lower energy barrier of 0.36 eV than that of HEA_{homo} (0.45 eV). The existence of FL-Ag enlarges the Ag–Ag ratios on FL-Ag/HEA surfaces, and the increased weak adsorption sites promote the $^*\text{NO}_3$ hydrogenation.

However, when the NitRR proceeds to the $^*\text{NO}$ hydrogenation step ($^*\text{NO}$ to $^*\text{NOH}$) on Ag sites, it requires a much higher energy barrier of 0.74 eV for $^*\text{NO}$ hydrogenation. Interestingly, it is shown that the $^*\text{NO}$ hydrogenation occurring on Pd sites of FL-Ag/HEA and HEA_{homo} are both spontaneous exothermic reactions with much lower energy barriers of ~ 1.23 and $\sim 1.02\text{ eV}$. Taking FL-Ag/HEA as an example, the conversion from $^*\text{NO}_3$ to $^*\text{NO}$ occurs on FL-Ag, and then, the as-formed $^*\text{NO}$ intermediates migrate from the FL-Ag to the neighboring Pd site on HEA–FL-Ag interfaces to finish the subsequent hydrogenation and NH_3 desorption processes. The in situ FTIR results also confirmed the existence of NO binding on the Pd site of FL-Ag/HEA (Fig. 5), supporting the contention that the NitRR pathways over FL-Ag/HEA exhibit a relay catalysis mechanism.

For NitRR, the HER is usually considered a competitive reaction, and actually, the HER is also an important H^+ source, which is required for the NitRR in an alkaline environment³⁸. In FL-Ag/HEA, although Ag sites have the lowest energy barrier for NO_3^- hydrogenation than other metals, and the high H_2O cleavage energy barrier at the Ag site ($>1.0\text{ eV}$) makes it difficult to proceed further $^*\text{NO}$ hydrogenation to NH_3 (Supplementary Note 4 and Supplementary Fig. 46). The electrochemical performance also confirmed that the Ag affords a high NO_2 yield rather than NH_3 yield (Fig. 4). The Fe sites in FL-Ag/HEA are the main active sites for HER with a small energy barrier of $<0.26\text{ eV}$ (Supplementary Fig. 48). The free energy diagram for the simultaneous NitRR and HER pathways on FL-Ag/HEA further shows that the HEA phase could regulate the HER to provide necessary H^+ while the FL-Ag uses free H^+ to promote the NitRR to generate NO_2/NO intermediates (Fig. 6c). Then, the generated $^*\text{NO}$ intermediates migrate from the FL-Ag to the neighboring Pd site on HEA–FL-Ag interfaces with low energy barriers to finish the subsequent hydrogenation and NH_3 desorption processes. The relay catalysis occurs on FL-Ag/HEA by promoting the NitRR and HER on different active sites, demonstrating the synergistic effects of the HEA and FL-Ag in ensuring sufficient H^+ production for the NitRR (Fig. 6d and Supplementary Fig. 48).

Discussion

We introduce a ‘surface entropy reduction’ strategy to design a FL-Ag/HEA electrocatalyst for NitRR. FL-Ag/HEA/CNFs exhibit a high NH_3 Faradaic efficiency of 92.7% , an NH_3 yield rate of $2.45\text{ mmol h}^{-1}\text{ mg}_{\text{cat}}^{-1}$, and notable long-term stability ($>200\text{ h}$), outperforming most of the state-of-the-art electrocatalysts and traditional Haber–Bosch process for NH_3 production (NH_3 yield rate = $0.2\text{ mmol h}^{-1}\text{ mg}_{\text{cat}}^{-1}$). Our experimental and calculation results highlight the importance and advantages of FL-Ag on HEA surfaces to improve the NitRR activity. Using the HEA and FL-Ag as separate active centers for deoxygenation and hydrogenation, respectively, relay catalysis can be performed on FL-Ag/HEA, where the conversion from $^*\text{NO}_3$ to $^*\text{NO}$ occurs on FL-Ag and the $^*\text{NO}$ intermediates migrate to the neighboring Pd site on HEA–FL-Ag interfaces for subsequent hydrogenation from $^*\text{NO}$ to NH_3 .

Methods

Synthesis of FeCoNiVAgPd FL-Ag/HEA and HEA_{homo} electrocatalysts

The synthesis procedure was according to our previous work⁶. Typically, 0.5 mmol of each metal salt and 2 g PAN power were dissolved into 22 g DMF to acquire a homogeneous solution. Afterward, the metal salts/PAN precursor nanofiber membranes were obtained via electrospinning (YFSP-T, Tianjin Yunfan Technology Co., Ltd). The nanofiber membrane was then transferred into the home-built chemical vapor deposition (CVD) furnace. The heating rate was set as 5°C min^{-1} . After pre-oxidation for 3 h , the materials were heated at 1000°C for 3 h under an Ar atmosphere. The FL-Ag/HEA/CNFs were obtained after naturally cooling to room temperature. By altering the calcination temperature, the HEA_{homo} /CNFs were successfully prepared.

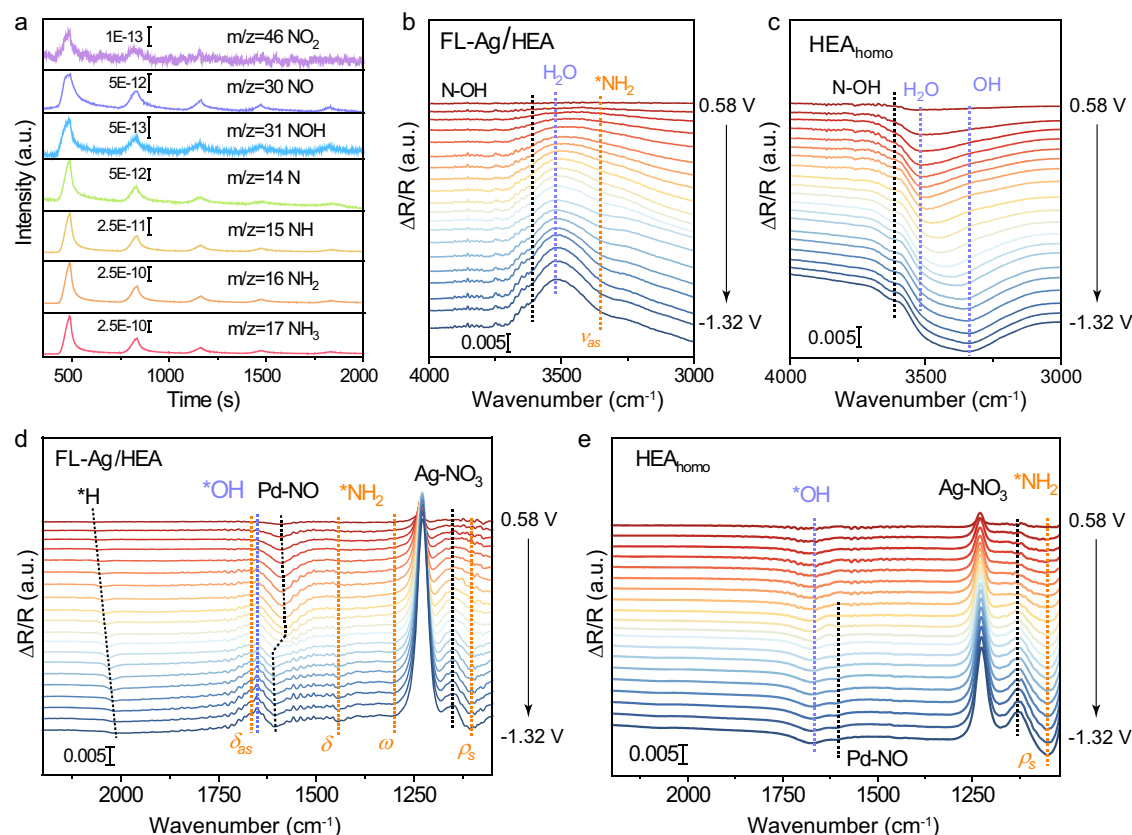


Fig. 5 | Investigations of the NitRR mechanism using operando spectroscopy. **a** Online DEMS spectra of the NitRR on FL-Ag/HEA/CNFs. Electrochemical in situ ATR-FTIR spectra of **(b, d)** FL-Ag/HEA/CNFs and **(c, e)** HEA_{homo}/CNFs during the NitRR.

Materials characterizations

The morphology of the as-synthesized catalysts was examined using FE-SEM (HITACHI S-4800) and aberration-corrected STEM (FEI-Titan Cubed Themis G2 300, Thermo Scientific). XAFS measurements were recorded in transmission mode at the BL14W1 station in the Shanghai Synchrotron Radiation Facility (SSRF). The acquired data was processed using Athena (version 0.9.26) for background removal, as well as pre-edge and post-edge calibration. Subsequently, Fourier transform fitting was performed using Artemis. The crystal structures were determined using an X-ray diffractometer (D8 ADVANCE, Bruker) with Cu K α radiation. Surface chemical states were obtained by XPS (Kratos Axis supra). The contents of metal elements were measured by ICP-OES (Agilent 5110). The gaseous and liquid products were examined using GC (Agilent 7890B) and ^1H NMR (Bruker Avance NEO 600).

Quantitatively analysis of surface atomic arrangement

The surface atomic arrangement was quantitatively processed by the StatSTEM software^{22,23}. For the pretreatment of the HAADF-STEM images with atomic resolution, the statistical parameter estimation theory was used to quantitatively determine the position of atomic columns. According to the intensities of the projected atomic columns, the superpositions of Gaussian peaks were generated after fitting the procedure to describe the measured position of atomic columns and accomplish the preliminary phase identification. To create the atomically resolved strain maps, the ideal crystal lattices of Ag and FeCoNiVAgPd HEA phases were preliminarily constructed from the XRD patterns with detailed Rietveld refinements and the Inorganic Crystal Structure Database. An atomic column in the unstrained region could be selected as the reference coordinate. A parameter-optimization treatment could be utilized to further refine the ideal

lattice parameters by fitting a larger unstrained area surrounding the selected reference coordinate. Based on the displacement between the detected position of the atomic column and the theoretical prediction, the atomical strain maps could be generated by processing the first derivatives of the displacement vectors.

Electrochemical measurements

The electrochemical measurements were performed in a typical H-type cell separated by the Nafion 117 membrane (183 μm), and the tests were collected by an electrochemical workstation (Autolab, PGSTAT302N). The as-prepared samples, saturated calomel electrode (SCE), and graphite rod were used as working electrode (WE), reference electrode (RE), and counter electrode (CE), respectively. The Nafion 117 membrane was pre-treated according to the literatures³. For the test, a 40 mL solution containing 0.5 M K₂SO₄ and 0.1 M KNO₃ (pH = 8.2 \pm 0.02, resistance = 8.81 \pm 0.37 Ω) was used as the cathode and anode electrolyte. Before each test, the compartments were saturated by Ar, and the RE was calibrated. The potentials *versus* SCE (E_{SCE}) were transformed into the potentials *versus* RHE (E_{RHE}) through the equation of $E_{\text{RHE}} = E_{\text{SCE}} + 0.244 + 0.059 \times \text{pH}$. The LSV curves were collected at a scan rate of 5 mV s⁻¹ without iR-compensation. The electrochemical active surface area (ECSA) was determined by

$$\text{ECSA} = C_{\text{dl}} / C_s \quad (1)$$

where the C_{dl} and C_s represent the electrochemical double layer capacitances (C_{dl}) and specific capacitance value (0.04 mF cm⁻²). The C_{dl} was obtained by

$$C_{\text{dl}} = (J_a - J_c) / 2\nu \quad (2)$$

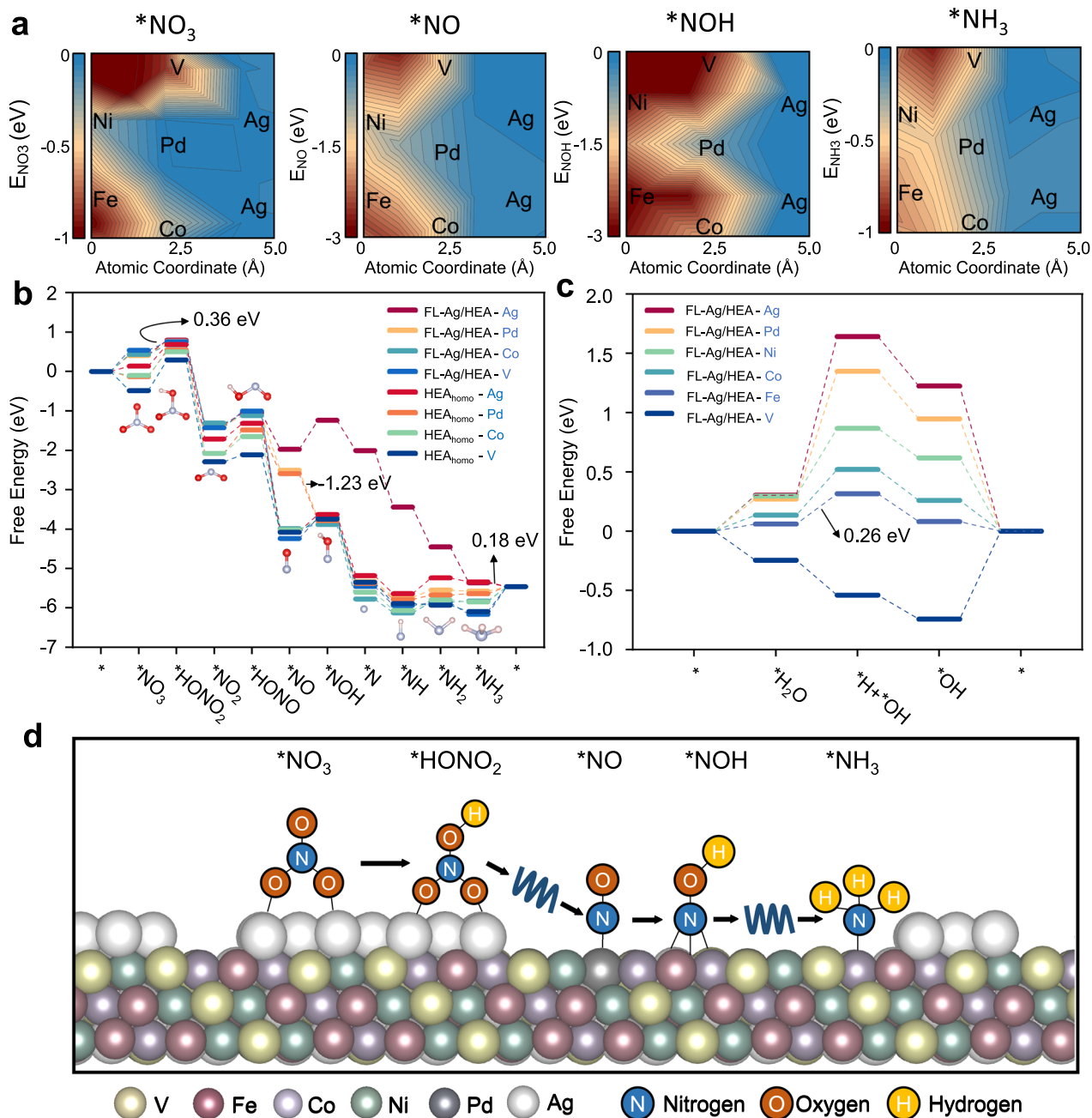


Fig. 6 | Theoretical calculations. **a** Adsorption energy distribution (E_i , $i = NO_3$, NO , NOH , and NH_3) of the intermediates on the FL-Ag/HEA surface. The lowest point of the adsorption energy was taken as 0, and then the relative values were calculated.

Reaction-free energies for the **(b)** NitRR and **(c)** HER on different metal sites in FL-Ag/HEA and HEA_{homo}. **d** Relay catalysis mechanism of NitRR over FL-Ag/HEA.

where the J_a and J_c are the positive and negative geometric current density of the CV cycles performed at various scan rates (ν). For the comparison, the mass activity was measured by depositing 5 μ L catalyst ink (3 mg catalyst powder, 750 μ L isopropanol, 250 μ L water, 25 μ L Nafion 117 solution) on the glassy carbon electrode (GCE, 3 mm). Chronoamperometry was employed for quantitative measurements and durability assessment.

Electrochemical in situ online DEMS measurements

Online DEMS was conducted using a QAS100 (Shanghai Linglu Instruments). The electrolyte for the electrochemical cell typically consisted of Ar-saturated 0.5 M K_2SO_4 and 0.1 M KNO_3 .

An Ag/AgCl electrode served as the RE, while a platinum wire acted as the CE, and a GCE modified with FL-Ag/HEA/CNFs functioned

as the WE. A waterproof polytetrafluoroethylene (PTFE) film (Shanghai Linglu Instruments) with a porosity of $\geq 50\%$ and a pore diameter of ≤ 20 nm was utilized. LSV measurements were acquired at a scan rate of 6 mV s⁻¹ over a potential range of 0.09 to -0.9 V vs. RHE for five cycles to investigate the generated intermediates and products.

Electrochemical in situ ATR-SEIRAS measurements

The ATR-SEIRAS measurements were conducted by a Thermo Nicolet 8700 spectrometer equipped with MCT detector cooled by liquid nitrogen. The Ar-saturated 0.5 M K_2SO_4 and 0.1 M KNO_3 were used as electrolytes. The Ag/AgCl electrode and Pt wire served as the RE and CE. For the preparation of WE, after the surface polishing by diamond suspension and cleaning in ultrapure water by sonication, the Si prism for IR reflection was covered by Au thin film (~60 nm) by a chemical

deposition process²⁷. The data were collected with a spectral resolution of 1 cm^{-1} and were analyzed by: $\text{DR}/R = (R_S - R_{\text{REF}})/R_{\text{REF}}$, where R_S and R_{REF} represent the FTIR spectra acquired at working potential and reference potential, respectively. The spectra collected at -0.68 V vs. RHE were taken as the R_{REF} , while the spectra of R_S were measured after applying the potential for 5 min.

Electrochemical in situ Raman measurements

The in situ Raman spectra were acquired in a well-designed electrolyzer (Beijing Scistar Technology Co., Ltd.) placed in the Raman spectrometer (inVia) with the laser of 785 nm . 10 mL of Ar-saturated $0.5\text{ M K}_2\text{SO}_4$ or Ar-saturated $0.5\text{ M K}_2\text{SO}_4$ and 0.1 M KNO_3 were used as electrolyte. The Ag/AgCl electrode and Pt wire were used as RE and CE, respectively. After the gold sputtering, the GCE was loaded with catalyst and served as the WE. Afterward, Raman spectra were collected after applying the working potentials for 2 min.

Quantitative detection of products

Indophenol blue method and nuclear magnetic resonance spectroscopy ($^1\text{H NMR}$) were used to determine the NH_3 products. For the typical indophenol blue method, $400\text{ }\mu\text{L}$ mixed solution containing 1.0 M NaOH , $5\text{ wt}\%$ salicylic acid, and $5\text{ wt}\%$ sodium citrate, $200\text{ }\mu\text{L}$ 0.05 M NaClO , and $200\text{ }\mu\text{L}$ sodium nitroprusside were successively added to the 2 mL of diluted electrolyte after reaction³⁹. After preservation without light for 2 h, the absorbance at $\text{ca. } 655\text{ nm}$ was measured by the UV-vis spectrophotometer (TU-1950). The $^1\text{H NMR}$ spectra were collected by employing AVANCE NEO 600 MHz with water suppression and 256 scans. The $500\text{ }\mu\text{L}$ electrolyte containing $50\text{ }\mu\text{L DMSO-}d_6$ was used for the test. To certify the origin of ammonia products, the isotope labeling method was carried out using the $^{14}\text{NO}_3^-$ and $^{15}\text{NO}_3^-$ as resources. The FE and yield of ammonium were calculated according to the following equations:

$$\text{FE} = [8F \times c(\text{NH}_4^+) \times 40\text{ mL}] / Q, \quad (3)$$

$$\text{yield}_{\text{geo}} = [c(\text{NH}_4^+) \times 40\text{ mL}] / (2\text{ h} \times A_{\text{geo}}), \quad (4)$$

$$\text{yield}_{\text{mass}} = [c(\text{NH}_4^+) \times 40\text{ mL}] / (2\text{ h} \times m_{\text{cat}}), \quad (5)$$

$$m_{\text{cat}} = M \times \omega_{\text{metal}} \quad (6)$$

where F , $c(\text{NH}_4^+)$, Q , A_{geo} , m_{cat} , and ω_{metal} is Faraday constant (96485 C mol^{-1}), the concentration of ammonium, total charge of the reaction, area of the electrodes, and mass loading of the active component, and the mass fraction (15.27%) of the metallic components determined by the ICP-OES (Supplementary Table 1). M is the mass loading of the catalyst, and for self-supported electrode evaluation, the M can be determined by analytical balance, while for GCE evaluation, the M is a constant of 0.015 mg ($(5\text{ }\mu\text{L}/1000\text{ }\mu\text{L}) \times 3\text{ mg}$). The mass (M) of the self-supported FL-Ag/HEA/CNFs electrode (1 cm^2) is 0.48 mg , and the active metal component mass loading (m_{cat}) is 0.073 mg . According to Eqs. 4–6, the $\text{yield}_{\text{geo}}$ and $\text{yield}_{\text{mass}}$ were $0.29\text{ mmol h}^{-1}\text{ cm}^{-2}$ and $3.932\text{ mmol h}^{-1}\text{ mg}_{\text{cat}}^{-1}$, respectively. The M of FL-Ag/HEA/CNFs on GCE (0.07069 cm^2) is 0.015 mg and the m_{cat} is 0.0023 mg . For GCE evaluation, the $\text{yield}_{\text{geo}}$ and $\text{yield}_{\text{mass}}$ were $0.079\text{ mmol h}^{-1}\text{ cm}^{-2}$ and $2.45\text{ mmol h}^{-1}\text{ mg}_{\text{cat}}^{-1}$, respectively. The quantitative detection of NO_2^- was accomplished by the Griess method using the mixture of N -(1-Naphthyl)ethylenediamine dihydrochloride (0.08 g), sulfanilamide (1.6 g), H_3PO_4 (4 mL , 85%), and ultrapure water (20 mL) as the Griess reagent⁴⁰. For the UV-vis tests, 2 mL of tested electrolyte were diluted to a standard solution containing a certain amount of K_2NO_2 , which was mixed with $40\text{ }\mu\text{L}$ of Griess reagent. The

absorbance at $\text{ca. } 540\text{ nm}$ was collected after stewing for 15 min. Gas chromatography (Agilent 7890B) with a thermal conductivity detector (TCD) and flame ionization detector (FID) was adopted to determine the produced H_2 using Ar as carrier gas. The FE of various products and the yield for NH_4^+ were derived from at least three independent measurements.

DFT calculations

Theoretical calculations were carried out using the Vienna Ab-initio Simulation Package (VASP, ver. 6.4.1). The interactions of valence electrons were modeled with the projector augmented-wave (PAW) pseudopotential and the Perdew–Burke–Ernzerhof (PBE) functional was applied for the electron exchange–correlation descriptions within the generalized gradient approximation (GGA)⁴¹. A cut-off energy of 520 eV was utilized, with convergence criteria established at 10^{-6} eV for energy and 0.05 eV/\AA for forces. The DFT-D4 correction was implemented to account for van der Waals interactions, and spin polarization was included to describe the magnetic properties of the system. We used the (111) surface to model the surface, modeled by 3 thick layers of metal. Periodic slab models were used with a vacuum layer of 20 \AA between slabs to prevent interactions. Geometric optimization was performed for all adsorbates as well as the two outermost layers of the slab. A K-point sampling grid of $2 \times 3 \times 1$ was employed for all calculations. The free energy change (ΔG) for each step of the reaction was calculated using the following equation:

$$\Delta G = \Delta E + \Delta \text{ZPE} - T\Delta S - eU \quad (7)$$

The ΔE denotes the energy variation of the system resulting from each reaction step, both before and after the process, while ΔZPE indicates the change in zero-point energy. ΔS represents the entropy change associated with each reaction. During the vibrational analyzes, all slab atoms were held fixed. ($T = 298.15\text{ K}$) Here, U is the potential at the electrode, and e is the transferred charge ($U = 0\text{ V}$).

Using the stable molecules HNO_3 and H_2 in the gas phase ($\text{HNO}_3(\text{g})$ and $\text{H}_2(\text{g})$) and liquid H_2O ($\text{H}_2\text{O}(\text{l})$) to fit the calculation of the energy of ions involved in the reaction, such as NO_3^- and OH^- . The calculation formula is as follows²⁵:

$$\Delta G(^*\text{NO}_3) = G(^*\text{NO}_3) + \frac{1}{2}G(\text{H}_2) - G(^*) - G_{\text{gas}}(\text{HNO}_3) + 0.391\text{ eV} - eU \quad (8)$$

$$G(\text{OH}^-) = G(\text{H}_2\text{O}) - \frac{1}{2}G(\text{H}_2) \quad (9)$$

The energy of the molecules is calculated in a vacuum of $20\text{ \AA} \times 20\text{ \AA} \times 20\text{ \AA}$. The Gibbs free energy of $\text{HNO}_3(\text{g})$, $\text{H}_2(\text{g})$, $\text{NH}_3(\text{g})$, and $\text{H}_2\text{O}(\text{l})$ were obtained through vibrational analyzes, as shown in Supplementary Table 5.

The calculated electronic energies (E), zero-point energy corrections (ZPE), and entropy contribution (TS) for the intermediates involved in NitRR across various surfaces were provided in Supplementary Tables 6–8. The Gibbs free energies of NitRR, HER, and NitRR + HER were calculated and presented in Supplementary Tables 9–11.

Data availability

The experiment data which support the findings of this study are presented in this article and the Supplementary Information, and are available from the corresponding authors upon request. The source data underlying Figs. 1–6 and Figs. in SI are provided as a Source Data file. Source data are provided in this paper.

References

- Xie, Y. et al. High carbon utilization in CO₂ reduction to multi-carbon products in acidic media. *Nat. Catal.* **5**, 564–570 (2022).
- Wang, L. et al. The reformation of catalyst: From a trial-and-error synthesis to rational design. *Nano Res.* **17**, 3261–3301 (2023).
- Chen, G. F. et al. Electrochemical reduction of nitrate to ammonia via direct eight-electron transfer using a copper-molecular solid catalyst. *Nat. Energy* **5**, 605–613 (2020).
- Wang, P. et al. Breaking scaling relations to achieve low-temperature ammonia synthesis through LiH-mediated nitrogen transfer and hydrogenation. *Nat. Chem.* **9**, 64–70 (2017).
- Zhao, Z. J. et al. Theory-guided design of catalytic materials using scaling relationships and reactivity descriptors. *Nat. Rev. Mater.* **4**, 792–804 (2019).
- Hao, J. et al. Unraveling the electronegativity-dominated intermediate adsorption on high-entropy alloy electrocatalysts. *Nat. Commun.* **13**, 2662 (2022).
- Gan, T. & Wang, D. Atomically dispersed materials: Ideal catalysts in atomic era. *Nano Res.* **17**, 18–38 (2024).
- Li, W. H., Yang, J. & Wang, D. Long-range interactions in diatomic catalysts boosting electrocatalysis. *Angew. Chem. Int. Ed.* **61**, e202213318 (2022).
- Löffler, T., Ludwig, A., Rossmeisl, J. & Schuhmann, W. What makes high-entropy alloys exceptional electrocatalysts? *Angew. Chem. Int. Ed.* **60**, 26894–26903 (2021).
- Yao, Y. et al. Carbothermal shock synthesis of high-entropy-alloy nanoparticles. *Science* **359**, 1489–1494 (2018).
- Yao, Y. et al. High-throughput, combinatorial synthesis of multi-metallic nanoclusters. *Proc. Natl. Acad. Sci. USA* **117**, 6316–6322 (2020).
- Pedersen, J. K., Batchelor, T. A. A., Bagger, A. & Rossmeisl, J. High-entropy alloys as catalysts for the CO₂ and CO reduction reactions. *ACS Catal.* **10**, 2169–2176 (2020).
- Wang, B. et al. General synthesis of high-entropy alloy and ceramic nanoparticles in nanoseconds. *Nat. Synth.* **1**, 138–146 (2022).
- Liu, Y. H. et al. Toward controllable and predictable synthesis of high-entropy alloy nanocrystals. *Sci. Adv.* **9**, eadf9931 (2023).
- Zhang, D. et al. Multi-site electrocatalysts boost pH-universal nitrogen reduction by high-entropy alloys. *Adv. Funct. Mater.* **31**, 2006939 (2021).
- Zhu, H. et al. A high-entropy atomic environment converts inactive to active sites for electrocatalysis. *Energy Environ. Sci.* **16**, 619–628 (2023).
- Glasscott, M. W. et al. Electrosynthesis of high-entropy metallic glass nanoparticles for designer, multi-functional electrocatalysis. *Nat. Commun.* **10**, 2650 (2019).
- Cui, M. et al. Multi-principal elemental intermetallic nanoparticles synthesized via a disorder-to-order transition. *Sci. Adv.* **8**, eabm4322 (2022).
- Batchelor, T. A. A. et al. High-entropy alloys as a discovery platform for electrocatalysis. *Joule* **3**, 834–845 (2019).
- Ding, Q. et al. Tuning element distribution, structure and properties by composition in high-entropy alloys. *Nature* **574**, 223–227 (2019).
- Karamad, M., Gonçalves, T. J., Jimenez-Villegas, S., Gates, I. D. & Siahrostami, S. Why copper catalyzes electrochemical reduction of nitrate to ammonia. *Faraday Discuss.* **243**, 502–519 (2023).
- Monai, M. et al. Restructuring of titanium oxide overlayers over nickel nanoparticles during catalysis. *Science* **380**, 644–651 (2023).
- de Backer, A., van den Bos, K. H. W., Van den Broek, W., Sijbers, J. & Van Aert, S. StatSTEM: An efficient approach for accurate and precise model-based quantification of atomic resolution electron microscopy images. *Ultramicroscopy* **171**, 104–116 (2016).
- Li, P. et al. Pulsed nitrate-to-ammonia electroreduction facilitated by tandem catalysis of nitrite intermediates. *J. Am. Chem. Soc.* **145**, 6471–6479 (2023).
- Fang, J. Y. et al. Ampere-level current density ammonia electrochemical synthesis using CuCo nanosheets simulating nitrite reductase bifunctional nature. *Nat. Commun.* **13**, 7899 (2022).
- Haber, F. & Le Rossignol, R. Über die technische darstellung von ammoniak aus den elementen. *Z. Elektrochem. Angew. Phys. Chem.* **19**, 53–72 (1913).
- Han, S. et al. Ultralow overpotential nitrate reduction to ammonia via a three-step relay mechanism. *Nat. Catal.* **6**, 402–414 (2023).
- Katturi, N. K., Ganeshamandiram, S. D., Kommu, N., Podagatlapalli, G. K. & Soma, V. R. Ultrafast coherent anti-Stokes Raman spectroscopic studies of nitro/nitrogen rich aryl-tetrazole derivatives. *Chem. Phys. Lett.* **756**, 137843 (2020).
- Manfait, M., Alix, A. J. P. & Delaunay-Zeches, J. Raman and infrared spectra of the square planar tetraamine palladium(II) chloride and its deuterate. *Inorg. Chim. Acta* **44**, L261–L264 (1980).
- Yao, Y., Zhu, S., Wang, H., Li, H. & Shao, M. A spectroscopic study on the nitrogen electrochemical reduction reaction on gold and platinum surfaces. *J. Am. Chem. Soc.* **140**, 1496–1501 (2018).
- Chen, F. et al. Blocking the sulfonate group in Nafion to unlock platinum's activity in membrane electrode assemblies. *Nat. Catal.* **6**, 392–401 (2023).
- Zhu, S. et al. The role of ruthenium in improving the kinetics of hydrogen oxidation and evolution reactions of platinum. *Nat. Catal.* **4**, 711–718 (2021).
- Lv, C. et al. Selective electrocatalytic synthesis of urea with nitrate and carbon dioxide. *Nat. Sustain.* **4**, 868–876 (2021).
- Brown, W. A., Gardner, P. & King, D. A. The adsorption of NO₂ on Ag {111}: a low temperature RAIRS study. *Surf. Sci.* **330**, 41–47 (1995).
- Müslühiddinoğlu, J. & Vannice, M. A. Adsorption of NO on promoted Ag/α-Al₂O₃ catalysts. *J. Catal.* **217**, 442–456 (2003).
- Di Monte, R. et al. NO reduction by CO over Pd/Ce_{0.6}Zr_{0.4}O₂–Al₂O₃ catalysts: in situ FT-IR studies of NO and CO adsorption. *Inorg. Chim. Acta* **334**, 318–326 (2002).
- Almusaiteer, K. & Chuang, S. S. C. Dynamic behavior of adsorbed NO and CO under transient conditions on Pd/Al₂O₃. *J. Catal.* **184**, 189–201 (1999).
- Liu, H. et al. Electrocatalytic nitrate reduction on oxide-derived silver with tunable selectivity to nitrite and ammonia. *ACS Catal.* **11**, 8431–8442 (2021).
- Zhu, D., Zhang, L., Ruther, R. E. & Hamers, R. J. Photo-illuminated diamond as a solid-state source of solvated electrons in water for nitrogen reduction. *Nat. Mater.* **12**, 836–841 (2013).
- Chen, F. Y. et al. Efficient conversion of low-concentration nitrate sources into ammonia on a Ru-dispersed Cu nanowire electrocatalyst. *Nat. Nanotechnol.* **17**, 759–767 (2022).
- Kresse, G. & Furthmüller, J. Efficient iterative schemes for ab initio total-energy calculations using a plane-wave basis set. *Phys. Rev. B* **54**, 11169 (1996).

Acknowledgements

This study was supported by the National Natural Science Foundation of China (NSFC) (52273058, 52073124, 22209073, 52072261, U22A20146), the Natural Science Foundation of Jiangsu Province (BK2022030167, BK20220912), the Postgraduate Research & Practice Innovation Program of Jiangsu Province (KYCX23_2465) and the Fundamental Research Funds for the Central Universities. The authors would also like to thank the Central Laboratory, School of Chemical and Material Engineering, and the BL14W1 station in Shanghai Synchrotron Radiation Facility (SSRF) for XAFS measurement.

Author contributions

H.Z. conceived the idea and designed the experiments. H.Z., G.G., Z.Z., and D.W. supervised the project. H.Z. and J.H. planned and performed the experiments. R.Y. and J.W. contributed to the structural analysis. G.G., T.W., and G.W. performed the theoretical calculations. J.C., S.L.,

M.D., Z.L., and Q.K. helped with the synthesis and characterization of the HEA. H.Z., Z.Z., G.G., and D.W. edited the paper, and all authors discussed the results and commented on the manuscript.

Competing interests

The authors declare no competing interests.

Additional information

Supplementary information The online version contains supplementary material available at

<https://doi.org/10.1038/s41467-024-53427-7>.

Correspondence and requests for materials should be addressed to Guohua Gao, Zechao Zhuang, Dingsheng Wang or Han Zhu.

Peer review information *Nature Communications* thanks the anonymous reviewer(s) for their contribution to the peer review of this work. A peer review file is available.

Reprints and permissions information is available at <http://www.nature.com/reprints>

Publisher's note Springer Nature remains neutral with regard to jurisdictional claims in published maps and institutional affiliations.

Open Access This article is licensed under a Creative Commons Attribution-NonCommercial-NoDerivatives 4.0 International License, which permits any non-commercial use, sharing, distribution and reproduction in any medium or format, as long as you give appropriate credit to the original author(s) and the source, provide a link to the Creative Commons licence, and indicate if you modified the licensed material. You do not have permission under this licence to share adapted material derived from this article or parts of it. The images or other third party material in this article are included in the article's Creative Commons licence, unless indicated otherwise in a credit line to the material. If material is not included in the article's Creative Commons licence and your intended use is not permitted by statutory regulation or exceeds the permitted use, you will need to obtain permission directly from the copyright holder. To view a copy of this licence, visit <http://creativecommons.org/licenses/by-nc-nd/4.0/>.

© The Author(s) 2024